Materials Research Express

OPEN ACCESS

RECEIVED
8 August 2025

REVISED
3 November 2025

ACCEPTED FOR PUBLICATION
6 November 2025

PUBLISHED
24 November 2025

PAPER

The role of processing parameters on the optoelectronic properties of TiO_2/MWCNT nanocomposites fabricated by sol-gel spin coating

Emin Yakar*

Materials Science and Engineering Department, Engineering Faculty, Canakkale Onsekiz Mart University, Canakkale, Turkiye

* Author to whom any correspondence should be addressed.

E-mail: eyakar@comu.edu.tr

Keywords: thin films, opto-electronic, spin coating, carbonecous materials, nanomaterials

Abstract

This study presents a systematic investigation into the influence of an optimized multi-step spin-coating process on the structural, optical, and electrical properties of TiO_2/multi-walled carbon nanotube (MWCNT) nanocomposite films deposited on indium tin oxide (ITO) substrates. A stable sol was synthesized using polyvinylidene fluoride (PVDF) as a binding agent. Structural characterization via x-ray diffraction (XRD) revealed that the optimized coating process resulted in an increase in the average crystallite size from 65 nm to 74 nm. Field-emission scanning electron microscopy (FE-SEM) and atomic force microscopy (AFM) analyses showed rough, heterogeneous surfaces with a non-uniform distribution of TiO_2 nanoparticles on the MWCNT network. The optical band gap energy was observed to increase from 2.88 eV to 3.06 eV following the additional spin-coating steps, which is attributed to enhanced electron localization and strong interfacial interactions. Current–voltage (I-V) measurements demonstrated non-linear and symmetrical behavior for both samples. The sample prepared with the standard process (TM1) exhibited a higher resistivity of 23.6 kΩ, attributed to defect complexes, while the sample with the optimized process (TM2) showed a lower resistivity of 18.6 kΩ, indicative of improved conductivity facilitated by effective MWCNT pathways and TiO_2 incorporation. This conclusion is supported by lower non-linear coefficients (α) of 1.85 and 1.52 for TM1 and TM2, respectively, suggesting trap-assisted electron transport governed by the Poole–Frenkel mechanism. The findings confirm that the electrical conductivity and overall optoelectronic performance of TiO_2/MWCNT nanocomposites can be significantly enhanced by tailoring the spin-coating parameters, primarily due to improved charge transport and suppressed electron–hole recombination.

1. Introduction

Metal oxides (e.g., SnO_2, ZnO, NiO) have garnered significant attention for their potential to replace conventional crystalline silicon and III-V compounds in various optoelectronic applications, owing to their abundance and tunable properties [1]. Among them, titanium dioxide (TiO_2) has been extensively studied due to its exceptional optoelectronic characteristics, including a high refractive index, excellent chemical stability, strong UV absorption, and notable photocatalytic activity. Its well-positioned conduction and valence bands make it a promising material for solar cells, sensors, and photoelectrochemical devices [2]. TiO_2 thin films commonly exist in two primary crystalline phases: anatase and rutile. The rutile phase, generally considered the most thermodynamically stable, requires higher energy to form from an amorphous state and plays a critical role in developing protective layers for optical applications [3]. The theoretical optical band gaps for rutile and anatase are approximately 3.00 eV and 3.20 eV, respectively. However, the wide band gap and rapid electron–hole recombination inherent to TiO_{22} can limit its efficiency in optoelectronic applications [4].

To address these limitations, researchers have developed TiO_2-based nanocomposites incorporating carbon nanomaterials such as graphene, single-walled carbon nanotubes (SWCNTs), and carbon fibers to

maximize surface area and minimize charge diffusion pathways [5]. In particular, multi-walled carbon nanotubes (MWCNTs) have been integrated into TiO_2 matrices to enhance charge transport, mechanical strength, and light absorption capabilities [6]. MWCNTs provide a highly conductive network that facilitates efficient electron transfer while suppressing charge recombination, thereby significantly improving the overall optoelectronic performance of the composite films [7]. For instance, using a solution casting method, Khan *et al* reported a decrease in the optical band gap from 4.79 eV for pure PVA to 3.6 eV for a PVA/TiO_2@MWCNT composite film with increasing MWCNT content [8]. Similarly, Akkari *et al* observed that while pure CNTs exhibited a band gap of 2.8 eV, the TiO_2/MWCNT nanocomposite showed a band gap of 3.1 eV [9].

The deposition technique is a crucial factor determining the structural and optoelectronic properties of thin films. Spin coating is a widely adopted method due to its simplicity, cost-effectiveness, and ability to produce uniform films with controllable thickness [10]. However, the properties of spin-coated TiO_{22}/MWCNT nanocomposites are highly sensitive to processing parameters such as spin speed, acceleration, solution concentration, and annealing conditions [11]. Previous studies have demonstrated that optimizing these parameters can profoundly influence film morphology, crystallite size, and electrical conductivity [12]. For example, Aydin *et al* demonstrated that a 2.1-MWCNT.In_2O_3/TiO_2-NTs composite exhibited the lowest resistance and highest performance due to synergistic effects, achieved via optimized spin coating [10]. Gui *et al* found that TiO_2 core–shell MWCNT nanocomposites exhibited excellent visible light absorption, with the absorption edge extending into the 380–600 nm range, depending on the MWCNT loading [11]. Despite these advancements, a systematic investigation into the specific effects of multi-step spin-coating processes on the optoelectronic properties of TiO_2/MWCNT films remains largely unexplored.

In this study, we investigate the impact of an optimized multi-step spin-coating process on the properties of TiO_2/MWCNT nanocomposite films deposited on ITO substrates. Through comprehensive analysis of structural modifications, charge transport behavior, and recombination dynamics, we demonstrate that the optimized coating process enhances electrical conductivity, improves light absorption, and increases electron mobility. The novelty of this work lies in the detailed analysis of how sequential spin-coating steps affect the nanocomposite's properties. We demonstrate that this specific optimization of processing parameters is a critical and effective tool for tailoring the structural, optical, and electrical properties of TiO_2/MWCNT films for enhanced performance, a aspect that remains underexplored for this specific synthesis method. Despite these advances, a systematic investigation into how sequential spin-coating and annealing conditions affect the optoelectronic properties of sol–gel derived TiO_2/MWCNT films remains unexplored. While spin coating is a known technique, the novelty of this work lies in the detailed analysis of how a multi-step processing protocol precisely tailors the interfacial structure, charge transport dynamics, and overall performance of the nanocomposite. By correlating specific processing steps with structural modifications (crystallite size, strain), optical characteristics (band gap, recombination), and electrical properties (conductivity, charge transport mechanism), this study establishes a refined process-structure–property relationship. This approach provides a new level of control over the material's properties, highlighting the potential of process optimization as a key design tool for enhancing performance in advanced optoelectronic applications such as photodetectors and sensors. While other deposition techniques such as screen printing are well-established for fabricating thick, large-area films with high throughput, the sol–gel spin-coating method offers distinct advantages for fundamental research and specific applications [13]. Spin coating provides superior control over film thickness at the nanoscale, allows for easy compositional variations, and facilitates the creation of highly homogeneous and smooth films, which are critical for detailed structure–property investigations and high-performance optoelectronic devices [14]. The focus of this work is to leverage this precise control to understand the fundamental impact of a multi-step spin-coating process on the material's properties.

2. Experimental

2.1. Materials

Indium tin oxide (ITO) substrates (25.4 mm × 76.2 mm × 1.2 mm) were used as the deposition surface. Titanium(IV) butoxide (97%, Sigma-Aldrich) was selected as the TiO_2 precursor. MWCNT powder was purchased from Nanografi, Turkey (>92% purity, external diameter: 8–10 nm, internal diameter: 5–15 nm, length: ~1–3 μm). Acetylacetone and absolute ethanol were employed as a stabilizer and solvent, respectively. All reagents were of analytical grade and were used without further purification.

2.2. Sample preparation

A standard substrate cleaning procedure was employed. The ITO substrates were sequentially ultrasonicated in acetone, distilled water, and ethanol for 10 min each at 30 °C. To prepare the sol, 0.05 g of MWCNT powder and a 0.1 M equivalent of titanium(IV) butoxide were dissolved in 20 ml of ethylene glycol. Then, 1.5 ml of

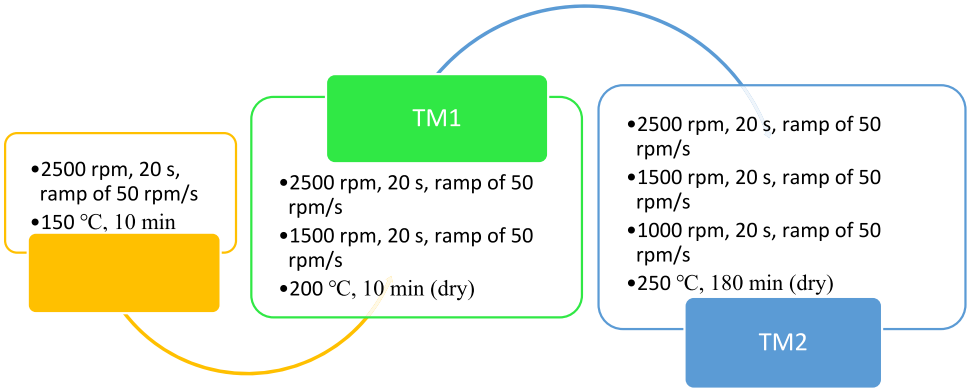

Scheme 1. Schematic illustration of the sol–gel spin-coating process for the fabrication of TM1 and TM2 samples.

isopropanol and 0.1 g of PVDF were added under constant stirring until a homogeneous solution was obtained. The resulting sol was aged for 4 days until it transitioned into a gel. The gel was then deposited onto the pre-cleaned ITO substrates using spin coating. The detailed procedures for fabricating the two samples, TM1 and TM2, are described in scheme 1.

2.3. Characterization

The crystalline phases of the coated films were analyzed by x-ray diffraction (XRD, Rigaku SmartLab) using Cu Kα radiation ($\lambda = 1.5406$ Å). Patterns were recorded in the 2θ range of 10° to 80° with a step size of 0.05°. Surface morphology and elemental composition were examined using field-emission scanning electron microscopy (FE-SEM, JEOL-7100F) operated at an accelerating voltage of 15.0 kV, coupled with energy-dispersive x-ray spectroscopy (EDAX, OXFORD Instruments X-Max). Surface topography was analyzed using an atomic force microscope (AFM, Witec alpha 300 RA) in non-contact mode. Contact angle measurements were performed by dispersing 5 µl droplets onto the film surfaces. Images were captured using a Canon 60D DSLR camera, and the contact angles were determined using standard software by averaging measurements from the left and right sides of at least three droplets. Raman spectra were acquired in the range of 100–3600 cm^{-1} using a 780 nm laser source (WITEC ALPHA 300RA). The electrical characterization was performed using a Keithley 4200-SCS parameter analyzer. Two-probe current–voltage (I-V) measurements were conducted with a voltage sweep from –2.0 V to +2.0 V to investigate the charge transport mechanism. Additionally, to determine the sheet resistance of the films independently of contact effects, four-point probe measurements were carried out in a linear configuration with equidistant probes, applying a known current and measuring the resulting voltage drop. Photoluminescence (PL) spectra were obtained using a CCD detector with an excitation wavelength of 325 nm in the range of 370–950 nm (Unidron RT-PL). UV–vis absorption spectra were measured in the wavelength range of 300–800 nm using a Shimadzu UV-1800 spectrophotometer. All measurements were conducted at room temperature.

3. Results and discussion

3.1. Structural properties

X-ray diffraction (XRD) is a powerful technique for determining the structural composition and crystallinity of materials. Figure 1 presents the XRD patterns of the TM1 and TM2 samples. The patterns were compared with the ICDD standard database, confirming the successful formation of the thin films.

The diffraction peaks observed at $2\theta = 27.4°$, 35.6°, 52.4°, and 55.4° correspond to the (110), (200), (211), and (220) planes of the rutile phase of TiO_2 (JPDS Card No: 21-1276), respectively. An additional peak at $2\theta = 38.7°$ is identified as the (002) plane of metallic titanium (JPDS Card No: 44-1294). The prevalence of the rutile phase, with its tetragonal structure, is significant as the high surface energy of the (211) plane promotes rapid crystal growth [15]. Notably, characteristic peaks of MWCNTs, typically expected in the 2θ range of 25°–30°, were not observed in either sample. This is likely due to the overwhelming intensity of the dominant TiO_2 (110) peak overshadowing the carbon signal [16]. Peaks corresponding to the In:SnO_2 (ITO) substrate were also detected at $2\theta = 62.4°$ and 66.3° (JPDS Card No: 72-1147), indicating a relatively thin coating layer.

The structural parameters of the TM1 and TM2 samples, detailed in table 1, were calculated from the XRD data. The average crystallite size (D) and intrinsic strain (ε) were estimated using the Williamson–Hall (W-H) method, as expressed in equation (1) [17]:

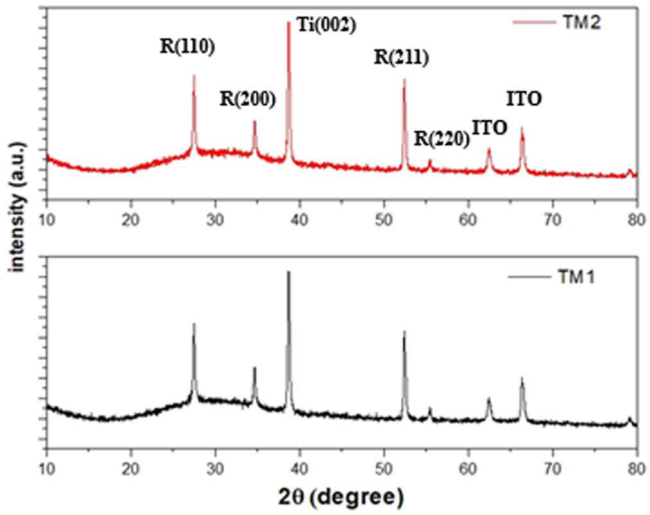

Figure 1. X-ray diffraction of TM1 and TM2 samples.

Table 1. Structural parameters of the TM1 and TM2 samples derived from XRD analysis.

	2θ(°)	d(Å)	FWHM	D(nm)	ε (10^{-3})	δ (10^{-4})	a = b (Å)	c (Å)
TM1	52.42	1.7440	0.1404	65	4.48	2.36	4.58	3.16
TM2	52.38	1.7450	0.1248	74	4.48	1.82	4.58	3.16

$$\beta \cos\theta = \frac{0.94\lambda}{D} + 4\varepsilon \sin\theta \tag{1}$$

where β is the full width at half maximum (FWHM) of the diffraction peak, θ is the Bragg angle, λ is the x-ray wavelength, D is the average crystallite size, and ε represents the strain. The dislocation density (δ), which signifies the number of defects in the crystal lattice, was calculated using equation (2):

$$\delta = 1/D^2 \tag{2}$$

The lattice parameters for the tetragonal phase were determined using equation (3):

$$\frac{1}{d^2} = \frac{h^2 + k^2}{a^2} + \frac{l^2}{c^2} \tag{3}$$

where a and c are the lattice parameters, (hkl) are the Miller indices, and d is the interplanar spacing.

As shown in table 1, the lattice parameter 'a' is consistent with standard values for rutile TiO_2 (a = b = 4.58 Å), while the 'c' parameter is slightly increased. This expansion may be attributed to the partial dissolution or interaction of MWCNTs with the TiO_2 crystal lattice [18]. Crucially, while the processing parameters did not alter the crystalline phase or induce significant strain, the average crystallite size increased from 65 nm in TM1 to 74 nm in TM2. This growth suggests that the additional spin-coating and thermal steps provide sufficient thermal energy for deposited atoms to migrate and integrate into existing grains rather than forming new, smaller nuclei [19].

3.2. Surface morphology

3.2.1. FE-SEM images of TiO_2/MWCNTs

Field-emission scanning electron microscopy (FE-SEM) was employed to examine the surface morphology of the TiO_2/MWCNT nanocomposites, as shown in figure 2. In both samples, the MWCNTs form an interconnected, network-like structure. TiO_2 nanoparticles with a grain-like morphology and an average particle size of approximately 50 nm are visible, distributed along the MWCNT surfaces.

A comparison between figure 2(a) (TM1) and figure 2(b) (TM2) reveals a notable difference in the surface topography and distribution of TiO_2. The TM2 sample, subjected to the multi-step spin-coating process, exhibits a more heterogeneous and rougher morphology. This suggests that the additional processing steps alter the deposition dynamics, leading to a more complex microstructure. The observed intimate contact between the TiO_2 nanoparticles and the MWCNT network in both samples is expected to facilitate electronic interaction, which is consistent with the enhanced electrical properties discussed in section 3.5 [20, 21]. This increased heterogeneity, while appearing as aggregation, is beneficial. It indicates a more intimate coupling between the

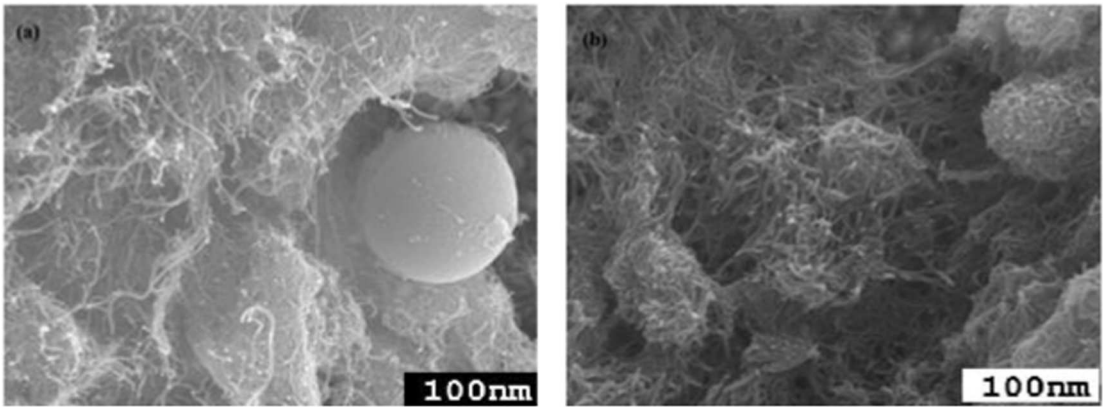

Figure 2. FE-SEM images of (a) TM1 and (b) TM2 surfaces at a high magnification of 30,000x.

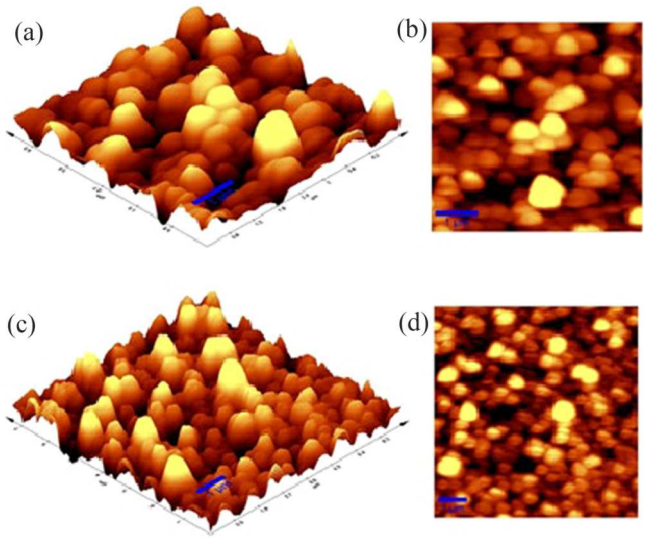

Figure 3. AFM images of the sample surfaces: (a) 3D view of TM1, (b) 2D view of TM1, (c) 3D view of TM2, (d) 2D view of TM2.

TiO_2 and the MWCNTs, which can significantly enhance the electronic and electrical properties of the nanocomposite by facilitating free electron transfer across the TiO_2-MWCNT interface [22].

3.2.2. AFM images of TiO_2/MWCNTs

The surface topography of the samples was further investigated using atomic force microscopy (AFM). The 3D and 2D AFM images for TM1 and TM2 are presented in figures 3(a)–(d). Both samples exhibit high surface roughness, a direct consequence of the incorporation and distribution of TiO_2 nanoparticles on the MWCNT scaffold [23].

The measured surface roughness values (S_a) for these films were in the ranges of 28–34 nm for TM1 and 31–37 nm for TM2. The slightly higher roughness observed for TM2 can be attributed to two main factors: limited surface diffusion due to the specific thermal budget of the process and the effect of larger crystallite size, as confirmed by XRD [24]. This result clearly demonstrates that modifying the spin-coating process directly influences the surface morphology and roughness of the resulting TiO_2/MWCNT films.

3.3. Raman spectrum of TiO_2/MWCNTs

Raman spectroscopy was employed to analyze the crystallinity and identify the chemical bonding and possible defects within the nanocomposites. The Raman spectra of the TM1 and TM2 samples are shown in figure 4.

The characteristic bands for the rutile phase of TiO_2 are visible at approximately 140 cm^{-1} ($B_{(1g)}$), 430 cm^{-1} (E_g), and 590 cm^{-1} (A_(1g)) [25]. The spectra also show the distinctive bands of MWCNTs: the D band at ~1345 cm^{-1}

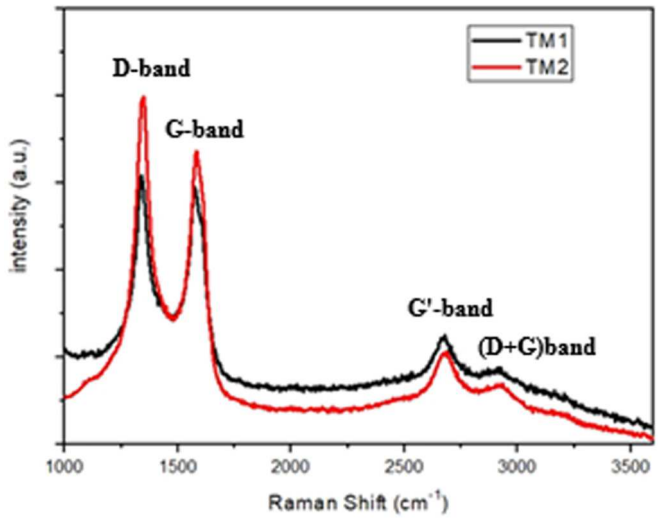

Figure 4. Raman spectra of TM1 and TM2 samples recorded in the 1000–3600 cm^{-1} range.

(disordered carbon mode), the G band at ~1585 cm^{-1} (tangential vibration mode of graphitic carbon), the 2D or G' band at ~2664 cm^{-1} (second-order overtone), and a combination band (D + G) at ~2912 cm^{-1} [26].

For the TM2 sample, a slight narrowing, a minor shift, and an increase in the intensity of these bands are observed. These changes can be attributed to the larger particle size and improved crystallinity, which enhance charge transfer from TiO_2 to the MWCNTs [27]. The intensity ratio of the D and G bands (I_D/I_G) is a key metric for quantifying defects in carbon materials. A value close to 1 indicates high-quality CNTs with few defects. The I_D/I_G ratio was found to increase in the TM2 sample, suggesting the introduction of sp^3 hybridized carbon defects on the MWCNT sidewalls during the additional processing steps. This indicates a higher degree of functionalization or interaction, which can improve the interfacial connection between the MWCNTs and TiO_2 [28, 29]. These Raman results are consistent with the findings from XRD, FE-SEM, and AFM, collectively confirming the successful formation of a TiO_2/MWCNT nanocomposite.

3.4. Optical properties

3.4.1. UV–vis spectrum of TiO_2/MWCNTs

The UV–vis absorption spectra of the TM1 and TM2 samples are presented in figures 5(a) and (b), respectively. While pure TiO_2 typically has an absorption edge around 355 nm (corresponding to its band gap), both nanocomposite samples exhibit a red-shifted absorption edge extending into the 380–400 nm range. This shift is caused by the excitation of electrons from the valence band to the conduction band of the TiO_2 matrix [30].

Notably, the TM2 sample shows a slight blue shift in its absorption edge compared to TM1. This phenomenon is attributed to the strong interfacial interaction between TiO_2 and the MWCNTs, enhanced by the optimized coating process. This interaction alters the surface charge properties of the TiO_2 particles, effectively increasing the band gap energy [31].

The optical band gap energies (E_g) for both samples were determined using the Tauc plot method, as expressed in equation (4):

$$(\alpha h\nu)^{1/n} = A(h\nu - E_g) \tag{4}$$

where α is the absorption coefficient, hν is the photon energy, A is a constant, and n defines the nature of the electronic transition (n = 1/2 for direct allowed transitions). The Tauc plots for TM1 and TM2 are shown in figures 5(c) and (d), respectively. The band gap energy increased from 2.88 eV for TM1 to 3.06 eV for TM2. This increase, known as a blue shift, suggests that electrons become more localized due to enhanced electronic coupling between TiO_2 and MWCNTs, which modifies the density of states near the band edges [32].

Our findings align with previous studies. For instance, Askari *et al* reported a band gap of 3.1 eV for a TiO_2/MWCNT nanocomposite [9], while Delekar *et al* observed a tunable band gap from 3.2 eV to 2.85 eV by varying the MWCNT content in TiO_2 [33].

3.4.2. Photoluminescence (PL) spectroscopy of TiO_2/MWCNTs

Photoluminescence spectroscopy was used to evaluate charge carrier recombination dynamics and identify surface defects, such as oxygen vacancies or trapped excitons, influenced by the incorporation of Ti^{4+} ions and MWCNTs [34]. The PL spectra of the TM1 and TM2 samples, excited at 325 nm, are shown in figure 6.

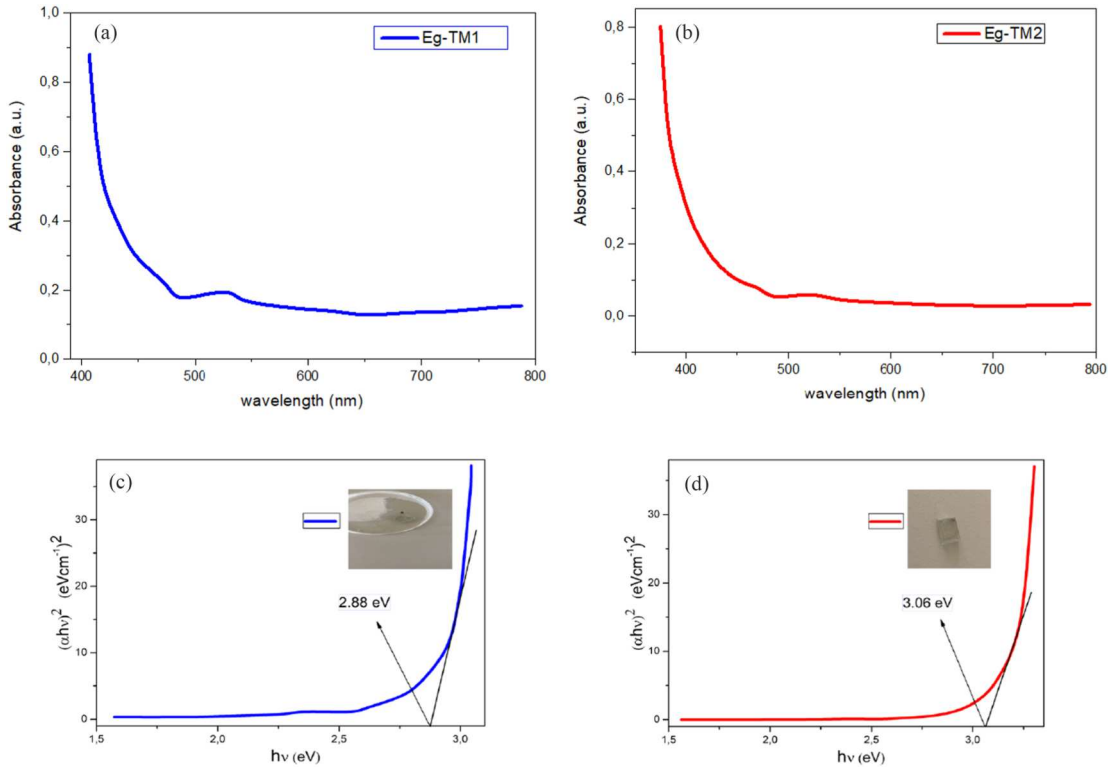

Figure 5. UV–vis absorption spectra of (a) TM1 and (b) TM2 samples. Tauc plots for determining the optical band gap of (c) TM1 and (d) TM2.

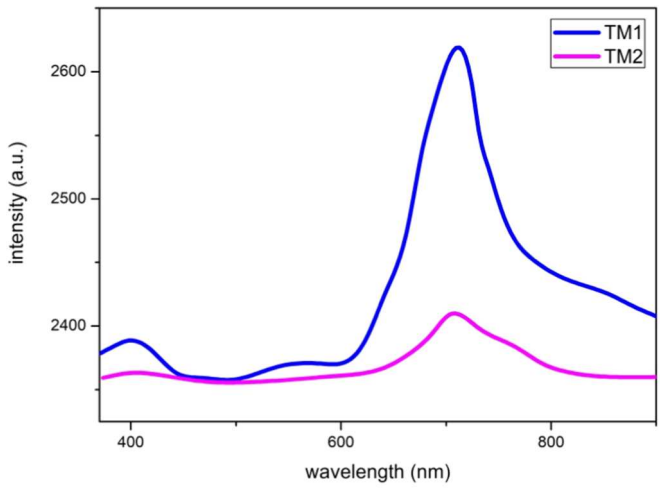

Figure 6. Photoluminescence spectra of TM1 and TM2 samples.

The TM1 sample exhibits two strong emission peaks at 399 nm and 711 nm. The peak at 399 nm is associated with band-to-band transitions in TiO_2, while the broader peak in the visible region (711 nm) is typically related to defect states and charge carrier recombination [35].

In contrast, the TM2 sample shows a significant quenching of the PL intensity and the emergence of a shallower peak around 705 nm. This suppression of PL emission is a strong indicator of reduced electron–hole recombination. In metal oxide-MWCNT composites, the PL quenching mechanism involves the transfer of photoexcited electrons from the conduction band of TiO_2 to the MWCNTs. The MWCNTs act as highly efficient electron acceptors and reservoirs, effectively scavenging electrons and thereby inhibiting the recombination process [36, 37]. This result confirms that the optimized spin-coating process in TM2 enhances the interfacial contact, leading to more efficient charge separation.

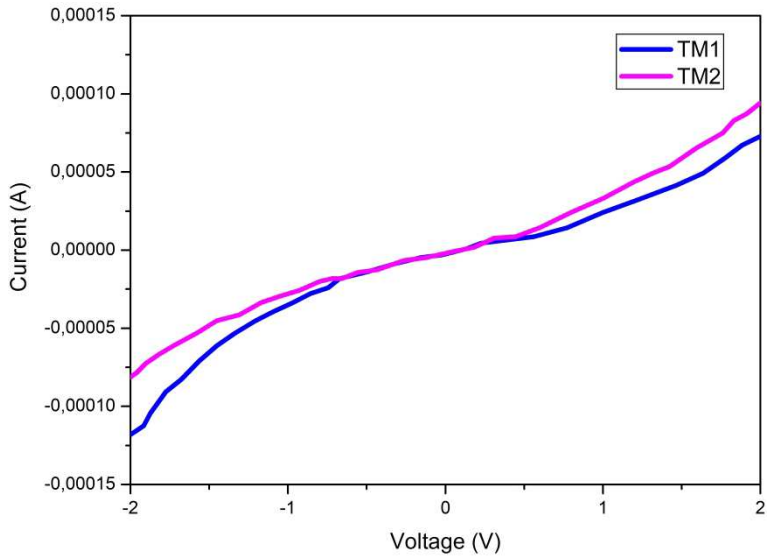

Figure 7. Current–Voltage (I-V) characteristics of TM1 and TM2 samples.

3.5. Electrical properties of TiO_2/MWCNTs

The current–voltage (I-V) characteristics of the TM1 and TM2 films are presented in figure 7. Both samples exhibit non-linear and symmetrical I-V curves, indicating non-ohmic (schottky-like) contact behavior.

The electrical resistivity, calculated from the slope of the I-V curves, was found to be 23.6 kΩ for TM1 and 18.6 kΩ for TM2. The higher resistivity of TM1 is likely due to a higher density of defect complexes that act as trapping centers for charge carriers . The decrease in resistivity for TM2 is attributed to the formation of improved conductive pathways through the MWCNT network and a more effective incorporation of TiO_2, which provides a higher concentration of mobile charge carriers [24]. The enhanced electrical conductivity of the TM2 film was further verified using the four-point probe technique, which mitigates contact resistance effects. The measured sheet resistance decreased from $\approx 2.4 \times 10^2\ \Omega\,\square^{-1}$ for TM1 to $\approx 1.9 \times 10^2\ \Omega\,\square^{-1}$ for TM2. This independent measurement corroborates the formation of superior, more homogeneous conductive pathways within the optimized nanocomposite, consistent with the I-V analysis.

To quantitatively describe the non-linear I-V behavior, the data was fitted to the power-law equation:

$$I = KV^{\alpha} \tag{5}$$

where K is a constant related to the material's conductivity, and α is the non-linear coefficient. The value of α was calculated using equation (6) [38]:

$$\alpha = \frac{(\log I_1 - \log I_2)}{(\log V_1 - \log V_2)} \tag{6}$$

The calculated non-linear coefficients were 1.85 for TM1 and 1.52 for TM2. These values greater than 1 confirm the non-ohmic conduction. The decrease in α for TM2 suggests a change in the conduction mechanism. The values are indicative of trap-assisted electron transport, where electrons are emitted from traps into the conduction band under an applied electric field, consistent with the Poole–Frenkel (PF) emission mechanism [39, 40].

The non-linear and symmetrical I-V characteristics can be comprehensively explained by the electronic interaction and energy level alignment at the TiO_2/MWCNT interface. The work function of metallic MWCNTs (typically ~4.8–5.0 eV) is higher than the electron affinity of TiO_2 (~4.2 eV) [41, 42]. This energy level alignment induces electron transfer from the TiO_2 conduction band to the MWCNTs upon contact, leading to the formation of a Schottky junction. The resulting band bending in TiO_2 creates an internal electric field that is highly efficient at separating photogenerated charge carriers. This mechanism provides a coherent explanation for the enhanced conductivity and the significant photoluminescence quenching observed in the TM2 sample. The observed symmetrical I-V response, rather than a rectifying one, is attributed to the percolative nature of the composite film, where the net electrical behavior is the sum of countless nanoscale Schottky junctions embedded within a conductive MWCNT network [43].

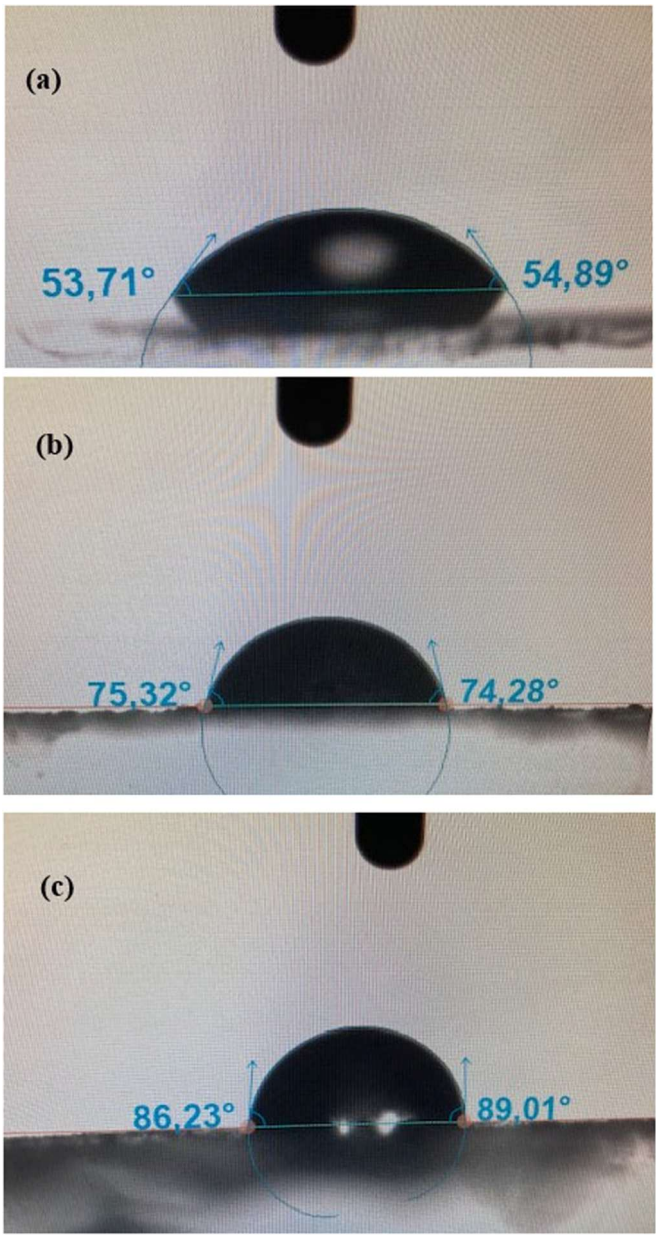

Figure 8. Contact angle images of a water droplet on (a) a bare ITO substrate, (b) TM1 surface, and (c) TM2 surface.

3.6. Surface wettability properties

The surface wettability of the films was assessed through water contact angle measurements, as shown in figures 8(a)–(c). The bare ITO substrate showed contact angles of approximately 54°. The TM1 film exhibited higher contact angles, around 75°, and the TM2 film showed the highest hydrophobicity with contact angles nearing 88°.

Both nanocomposite films demonstrated a transition towards more hydrophobic behavior compared to the bare ITO substrate. The increase in contact angle correlates well with the increase in surface roughness observed in the AFM analysis, following the Wenzel model, where roughness amplifies the intrinsic wetting behavior of a surface [44]. The TM2 sample, with the highest roughness, consequently shows the highest contact angle. This trend indicates that the surface energy decreases with the additional spin-coating process, making the surface less hydrophilic. Factors such as surface cracking, band gap energy, and particle size have also been reported to influence the hydrophilic/hydrophobic behavior of TiO_2-based films [45].

3.7. Discussion on electronic ınteraction and charge transfer

The enhancement in electrical conductivity (section 3.5) and the suppression of photoluminescence (section 3.4.2) observed in the TM2 sample strongly suggest efficient charge transfer at the TiO_2/MWCNT interface, which inhibits electron–hole recombination. The compelling enhancement in electrical conductivity

(section 3.5) and the significant suppression of photoluminescence (section 3.4.2) observed in the TM2 sample provide strong, indirect evidence for efficient charge transfer at the TiO_2/MWCNT interface, which inhibits electron–hole recombination. This experimental evidence is consistent with the well-established charge transfer mechanism reported in the literature for analogous nanocomposite systems. For instance, seminal work by Wang *et al* on MWCNT-TiO_2 composites prepared by a sol–gel method provided direct XPS evidence for this interaction, measured as a negative shift in the Ti 2p binding energy [46]. This shift is a recognized indicator of an increase in electron density on the Ti atoms, consistent with electron donation from the MWCNTs to the TiO_2 matrix. Similar XPS results, demonstrating modifications in the C 1s and Ti 2p spectra due to carbon-TiO_2 bonding and charge transfer, have been extensively reported in studies on carbon-based TiO_2 hybrids [41, 42]. The convergence of our optoelectrical findings with this established literature provides a robust foundation to conclude that the optimized multi-step process in TM2 successfully enhances this critical electronic interaction, with the MWCNT network acting as an efficient electron sink and highway.

The enhanced electrical and optoelectronic properties of our TM2 sample align perfectly with this established charge transfer mechanism. The MWCNT network likely acts as an efficient electron sink and highway, accepting photo-generated electrons from the TiO_2 conduction band, thereby facilitating prolonged charge separation and enhancing overall conductivity [41, 43].

3.8. Discussion on photocatalytic potential

Although demonstrating a specific photocatalytic reaction is beyond the scope of this study, the enhanced optoelectronic properties of the TM2 sample provide compelling and direct evidence of its strong potential for photocatalytic applications. The key requirements for efficient photocatalysis are met: enhanced visible light absorption (figure 5(b)), drastically suppressed electron–hole recombination as evidenced by significant PL quenching (figure 6), and improved charge carrier mobility indicated by lower resistivity (figure 7). The underlying mechanism, driven by the favorable band alignment at the TiO_2/MWCNT interface where MWCNTs act as electron sinks, is precisely the same mechanism responsible for enhanced photocatalytic activity in analogous composites reported in the literature. For instance, Woan *et al* directly linked this charge transfer to significantly higher photocatalytic degradation rates of organic dyes [43]. Similarly, Zhang *et al* reported superior gas-phase photocatalytic performance in TiO_2/graphene systems, which operate on an analogous principle [4]. Therefore, the optimized TM2 nanocomposite possesses the essential material characteristics for high photocatalytic performance, such as in pollutant degradation or water splitting. The process optimization strategy presented here serves as a foundation for future work focusing on varying MWCNT proportions to maximize photocatalytic efficiency.

3.9. Energy band alignment and charge transfer mechanism

To elucidate the origin of the enhanced electrical conductivity and efficient charge separation observed in the TM2 sample, an energy band alignment diagram for the TiO_2/MWCNT interface is proposed in figure 9, based on the experimental results and established literature. The electronic interaction at this heterojunction is governed by the relative work functions of the constituent materials.The work function (Φ) of metallic multi-walled carbon nanotubes is widely reported to be in the range of 4.8 to 5.0 eV [41, 42]. In contrast, the electron affinity (χ) of rutile TiO_2, which defines the energy level of its conduction band minimum (CBM) relative to the vacuum level, is approximately 4.2 eV. Before contact, the Fermi level (E_F) of the MWCNTs is therefore lower in energy (i.e., deeper) than the CBM of TiO_2. Upon intimate contact, thermodynamic equilibrium requires the unification of the Fermi levels across the system. This driving force prompts a spontaneous flow of electrons from the higher-energy CBM of TiO_2 to the lower-energy states of the MWCNTs, as indicated by the arrow in figure 9. This electron transfer has two critical consequences. First, it creates a space-charge region in the TiO_2, leading to a characteristic downward band bending near the interface. This bending establishes an internal electric field. Second, it results in the formation of a Schottky-like barrier (Φ_B) for electron injection from the MWCNTs back into the TiO_2, which was estimated to be 0.6–0.8 eV based on the energy difference between the final aligned Fermi level and the TiO_2 CBM at the interface. The observed non-linear yet symmetrical I-V characteristics (section 3.5) and the significant photoluminescence quenching (section 3.4.2) are direct consequences of this band alignment. The internal electric field facilitates the efficient separation of photogenerated electron–hole pairs, sweeping electrons toward the MWCNT network and holes toward the TiO_2 bulk, thereby drastically reducing recombination. The symmetrical electrical behavior, rather than classic rectification, is attributed to the percolative nature of the composite. The interconnected MWCNT network creates numerous parallel conduction pathways, effectively averaging out the individual nanoscale Schottky junctions and leading to the observed high, non-ohmic conductivity. This proposed mechanism, substantiated by the XRD, FE-SEM, UV–vis, PL, and I-V data, provides a coherent physical model for the superior optoelectronic performance of the TM2 sample fabricated via the optimized multi-step spin-coating process.

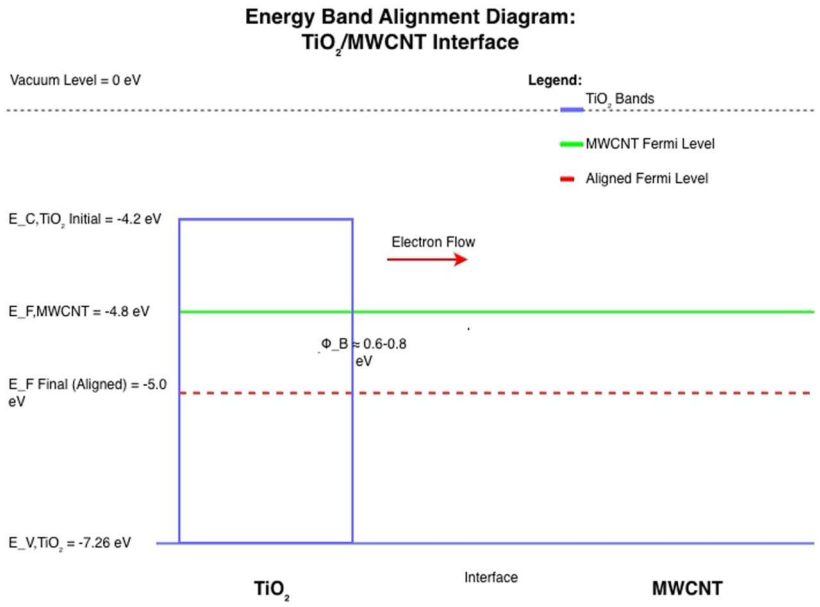

Figure 9. Energy band alignment diagram at the TiO_2/MWCNT interface.

The work function of MWCNTs (Φ_MWCNT ≈ 4.8–5.0 eV) is higher than the electron affinity of TiO_2 (χ_TiO_2 ≈ 4.2 eV). Upon contact, electron transfer from the TiO_2 conduction band to the MWCNTs occurs until Fermi level (E_F) alignment is achieved, resulting in band bending in TiO_2 and the creation of a Schottky-like barrier (Φ_B). This configuration promotes efficient charge separation and explains the enhanced conductivity and quenched photoluminescence observed in the TM2 nanocomposite.

4. Conclusion

In this study, TiO_2/MWCNT nanocomposite films were successfully synthesized on ITO substrates using a sol–gel spin-coating method. The profound impact of an optimized multi-step spin-coating process (TM2) on the structural, morphological, optoelectronic, and wetting properties was systematically investigated and compared to a standard process (TM1). The significantly enhanced charge separation, suppressed recombination, and tunable electrical conductivity achieved through the optimized coating process make these nanocomposites highly promising for advanced optoelectronic applications. Specifically, the demonstrated properties are directly relevant for use in high-performance photodetectors, (photo)electrochemical sensors, and as efficient charge-transport layers in solar cell architectures.

XRD analysis confirmed the formation of the rutile TiO_2 phase, with the optimized process leading to an increase in average crystallite size from 65 nm to 74 nm. Microscopy techniques (FE-SEM and AFM) revealed a rough, heterogeneous morphology with a non-uniform distribution of TiO_2 on the MWCNT network, with TM2 exhibiting higher surface roughness. Raman spectroscopy verified the presence of both components and indicated enhanced interfacial interaction in the TM2 sample. Optically, the band gap energy increased from 2.88 eV to 3.06 eV for TM2, attributed to strong interfacial coupling and electron localization. Crucially, significant PL quenching in the TM2 sample demonstrated a reduction in electron–hole recombination, implying more efficient charge separation. Electrically, the TM2 film showed a lower resistivity (18.6 kΩ) compared to TM1 (23.6 kΩ), due to the formation of superior conductive pathways via the MWCNT network. The enhancement in electrical conductivity, corroborated by a lower sheet resistance in the four-point probe measurement, underscores the efficacy of the optimized process in establishing superior charge transport pathways The non-linear I-V characteristics and the calculated coefficients suggested trap-assisted Poole–Frenkel conduction. Furthermore, the surface wettability transitioned to a more hydrophobic state for the nanocomposites, with TM2 showing the highest water contact angle due to its increased roughness. The enhanced hydrophobic character observed in the TM2 film suggests potential applicability in self-cleaning coatings, where a high water contact angle facilitates the removal of surface contaminants. The work function of MWCNTs (Φ_MWCNT ≈ 4.8–5.0 eV) is higher than the electron affinity of TiO_2 (χ_TiO_2 ≈ 4.2 eV). Upon contact, electron transfer from the TiO_2 conduction band to the MWCNTs occurs until Fermi level (E_F) alignment is achieved, resulting in band bending in TiO_2 and the creation of a Schottky-like barrier (Φ_B). This configuration promotes efficient

charge separation and explains the enhanced conductivity and quenched photoluminescence observed in the TM2 nanocomposite.

In summary, the optimized spin-coating process significantly enhances the optoelectronic performance of TiO_2/MWCNT nanocomposites by improving crystallinity, promoting efficient charge transfer, suppressing recombination, and increasing electrical conductivity. These tailored properties make these nanocomposites highly promising for advanced optoelectronic applications, including solar cells and photodetectors. Furthermore, the significantly enhanced charge separation and electron transport efficiency observed in the TM2 sample are fundamental prerequisites for superior photocatalytic performance. Based on the demonstrated optoelectronic properties and supported by literature on analogous composites [42, 43], our TiO_2/MWCNT films present a strong potential for application in photocatalytic systems, such as for the degradation of environmental pollutants.

Data availability statement

No new data were created or analysed in this study.

References

[1] Yu X, Marks T and Facchetti A 2016 Metal oxides for optoelectronic applications *Nature Mater* **15** 383–96
[2] Grätzel M 2001 Photoelectrochemical cells *Nature* **414** 338–44
[3] Chacko A, Hack E, Lohde S, Bucher R, Yildirim O, Mueller A and Dimitrievska M 2025 On tailoring structural and optoelectronic properties of TiO_2 thin films synthesized via 'room' temperature high power ımpulse magnetron sputtering *JPhys Energy* **7** 035017
[4] Zhang Y, Tang Z R, Fu X and Xu Y J 2010 TiO_2—graphene nanocomposites for gas-phase photocatalytic degradation of volatile aromatic pollutants *ACS Nano* **4** 7303–14
[5] Eder D 2010 Carbon nanotube—inorganic hybrids *Chem. Rev.* **110** 1348–85
[6] Lee J S, You K H and Park C B 2012 Highly photoactive TiO_2 nanotubes for hydrogen production by photocatalytic water splitting *Adv. Mater.* **24** 1084–8
[7] Norrman K, Ghanbari-Siahkali A and Larsen N B 2005 Studies of spin-coated polymer films *Annual Reports on the Progress of Chemistry, Section C* **101** 174–201
[8] Khan A, Khan S and Lee J 2020 Effect of TiO_2-coated MWCNTs on the optical properties of PVA films *J. Mater. Sci., Mater. Electron.* **31** 9876–85
[9] Askari M B, Tavakoli Banizi Z, Seifi M, Bagheri Dehaghi S and Veisi P 2017 Synthesis of TiO_2 nanoparticles and decorated multi-wall carbon nanotube (MWCNT) with anatase TiO_2 nanoparticles and study of optical properties and structural characterization of TiO_2/MWCNT nanocomposite *Optik* **149** 447–54
[10] Baran Aydın E and Sığırcık G 2025 Synthesis of TiO_2-NTs coated with MWCNT/In_2O_3-NRs: Investigation of efficiency in electrocatalytic hydrogen production *Inorg. Chem. Commun.* **178** 114476
[11] Gui M M, Chai S-P, Xu B-Q and Mohamed A R 2014 Visible-light-driven MWCNT@TiO_2 core–shell nanocomposites and the roles of MWCNTs on the surface chemistry, optical properties and reactivity in CO_2 photoreduction *RSC Adv.* **4** 24007–13
[12] Singh E and Nalwa H S 2015 Stability of graphene-based heterojunction solar cells *Journal of Materials Science & Technology* **31** 1076–82
[13] Brinker C J and Scherer G W 2013 *Sol-Gel Science: the Physics and Chemistry of Sol-Gel Processing* (Academic)
[14] Sadia S I, Shishir M K H, Ahmed S, Aidid A R, Islam M M, Rana M M and Alam M A 2024 Crystallographic biography on nanocrystalline phase of polymorphs titanium dioxide (TiO_2): a perspective static review *S. Afr. J. Chem. Eng.* **50** 51–64
[15] Singh A K, Vishwakarma P K, Pandey S K, Pratap R, Giri R and Srivastava A 2023 A comparative study of band gap engineered *in situ* and *ex situ* MWCNTs/TiO_2 heterostructures for their enhanced photocatalytic activity under visible light *Inorg. Chem. Commun.* **150** 110540
[16] Rabiei M, Palevicius A, Dashti A, Nasiri S, Monshi A, Doustmohammadi A and Janusas G 2021 X-ray diffraction analysis and Williamson-Hall method in USDM model for estimating more accurate values of stress-strain of unit cell and super cells ($2 \times 2 \times 2$) of Hydroxyapatite, confirmed by ultrasonic pulse-echo test *Materials* **14** 2949
[17] Özütok F, Er I K, Acar S and Demiri S 2019 Enhancing the Co gas sensing properties of ZnO thin films with the decoration of MWCNTs *J. Mater. Sci., Mater. Electron.* **30** 259–65
[18] Li J, Zhang H, Wang Z, Huang X and Zhang X 2024 Study on the grain development and dislocation evolution from dynamic to post-dynamic stage in IN718Plus superalloy; the role of second-phase *Mater. Charact.* **216** 114302
[19] Sabti H 2025 Effect of surface treatment of MWCNTs on the enhancement of the thermal and mechanical properties of aramid-MWCNT composites *J. Polym. Res.* **32** 70
[20] Kaushik P, Eliáš M, Prášek J, Michalička J and Zajíčková L 2021 Manipulating MWCNT/TiO_2 heterostructure morphology at nanoscale and its implications to NO2 sensing properties *Mater. Chem. Phys.* **271** 124901
[21] Prabakaran S, Nisha K D, Harish S, Hayakawa Y and Navaneethan M 2023 Boosting the electrical and charge transfer properties of TiO_2 by the effect of Mo doped and rGO nanocomposite *J. Alloys Compd.* **947** 169186
[22] Vrbová H, Kubišová M, Pata V, Knedlová J, Javořík J and Bočáková B 2024 Approach to heterogeneous surface roughness evaluation for surface coating preparation *Coatings* **14** 471
[23] Böer K W and Pohl U W 2022 Band-to-band transitions *Semiconductor Physics* 1–29
[24] Qu X and Wang H 2021 Power converters and control of LEDs *Control of Power Electronic Converters and Systems* 645–88
[25] Yakar E, Sarf F, Bayirli M and Ilgaz A 2024 Surface dynamics and electrochemical examination of Co3O4 films by iron doping *Surf. Topography: Metrol. Prop.* **12** 035025
[26] Challagulla S, Tarafder K, Ganesan R and Roy S 2017 Structure sensitive photocatalytic reduction of nitroarenes over TiO_2 *Sci. Rep.* **7** 8783

[27] Lee A Y, Yang K, Anh N D, Park C, Lee S M, Lee T G and Jeong M S 2021 Raman study of D* band in graphene oxide and its correlation with reduction *Appl. Surf. Sci.* **536** 147990
[28] Guan S, Cheng Y, Hao L, Yoshida H, Tarashima C, Zhan T and Lu Y 2023 Oxygen vacancies induced band gap narrowing for efficient visible-light response in carbon-doped TiO_2 *Sci. Rep.* **13** 14105
[29] Oktaviano H S, Yamada K and Waki K 2012 Nano-drilled multiwalled carbon nanotubes: characterizations and application for LIB anode materials *J. Mater. Chem.* **22** 25167
[30] Sharma H K, Sharma S K, Vemula K, Koirala A R, Yadav H M and Singh B P 2021 CNT facilitated interfacial charge transfer of TiO_2 nanocomposite for controlling the electron-hole recombination *Solid State Sci.* **112** 106492
[31] Kanmaz İ, Tomakin M, Aytemiz G, Manır M and Nevruzoğlu V 2024 Influence of thermal annealing on the band-gap of TiO_2 thin films produced by the sol-gel method *Recep Tayyip Erdoğan Üniversitesi Fen ve Mühendislik Bilimleri Dergisi* **5** 49–56
[32] Delekar S D, Dhodamani A G, More K V, Dongale T D, Kamat R K, Acquah S F A and Panda D K 2018 Structural and optical properties of nanocrystalline TiO_2 with multiwalled carbon nanotubes and its photovoltaic studies using Ru(II) sensitizers *ACS Omega* **3** 2743–56
[33] Gunkel F, Christensen D V, Chen Y Z and Pryds N 2020 Oxygen vacancies: the (in)visible friend of oxide electronics *Appl. Phys. Lett.* **116** 120505
[34] Al-Asbahi B A 2024 Charge transfer investigation in the nanocomposite of ZnO nanoparticles modified by multiwalled carbon nanotube *J. Inorg. Organomet. Polym. Mater.* **34** 313–21
[35] Gangu K K, Maddila S and Jonnalagadda S B 2019 A review on novel composites of MWCNTs mediated semiconducting materials as photocatalysts in water treatment *The Science of the Total Environment* **646** 1398–412
[36] Varghese D, Niranjana S R, Jennifer P J S, Muthupandi S, Madhavan J and Raj M V A 2025 Synergistic design of $CuO/CoFe_2O_4$/MWCNTs ternary nanocomposite for enhanced photocatalytic degradation of tetracycline under visible light *Sci. Rep.* **15** 320
[37] Karaduman Er İ, Sarf F and Yakar E 2022 Tuning optical and electrical properties of ultra-fast prepared nanoflower Mg:ZnO films by MWCNTs coating. *Bilge International Journal of Science and Technology Research* **6** 83–90
[38] Xiao M, Wang K, Chenyang X and Xie S 2014 Nonlinear current–voltage behavior of $CaCu_3Ti_4O_{12}$ thin films derived from sol–gel method *J. Mater. Sci., Mater. Electron.* **25** 2710–5
[39] El-naggar A A M, Alsulaymani L A, Alsaleh A A, Kamal A M and Albassam A A 2024 Exploring the optical and electrical features of PVA/CMC/PPy/MWCNTs blended polymers *Opt. Mater.* **155** 115878
[40] Wang W, Zhang J, Chen F, He D and Anpo M 2008 Preparation and photocatalytic properties of Fe^{3+}-doped TiO_2 nanoparticles *J. Colloid Interface Sci.* **323** 182–6
[41] Eder D 2010 Carbon nanotube–ınorganic hybrids *Chem. Rev.* **110** 1348–85
[42] Zhang Y, Tang Z-R, Fu X and Xu Y-J 2010 TiO_2—graphene nanocomposites for gas-phase photocatalytic degradation of volatile aromatic pollutant *ACS Nano* **4** 7303–14
[43] Woan K, Pyrgiotakis G and Sigmund W 2009 Photocatalytic carbon-nanotube–TiO_2 composites *Adv. Mater.* **21** 2233–9
[44] David Rathnaraj J, Dinesh C, Velmurugan R and Adithya A 2022 Effect of particle size on TiO_2-polystyrene nanoparticles contact angle for hydrophobicity behavior *Mater. Today Proc.* **66** 1107–11
[45] Momeni M, Saghafian H, Golestani-Fard F, Barati N and Khanahmadi A 2017 Effect of SiO_2 addition on photocatalytic activity, water contact angle and mechanical stability of visible light activated TiO_2 thin films applied on stainless steel by a sol gel method *Appl. Surf. Sci.* **392** 80–7
[46] Wang W, Serp P, Kalck P and Faria J L 2005 Visible light photodegradation of phenol on MWNT-TiO_2 composite catalysts prepared by a modified sol–gel method *J. Mol. Catal. A: Chem.* **235** 194–9